

MEMS Sensor Network for Submarine Terrain and Strata Deformation Monitoring: Design and Field Experiment

Yongqiang Ge^{ID}, Jiawang Chen^{ID}, Chen Cao^{ID}, Peng Zhou^{ID}, Chunying Xu^{ID}, Hai Zhu^{ID}, and Qixiao Zhou^{ID}

Abstract—The deformation monitoring of terrain and shallow strata is important to the gas hydrate mining environment and the early warning of seabed instabilities. Due to the complexity of the deep-sea environment and the difficulty of the seabed operation, in situ and high-precision deformation monitoring of terrain and shallow strata simultaneously are big challenges for existing observation methods. This article describes the design and experimental research of a terrain and strata deformation monitoring system based on micro-electromechanical system (MEMS) sensor network (SN). The SN consists of a horizontal array and a vertical array containing multiple cascaded MEMS accelerometers. The pitch angle and roll angle of the monitoring node can be calculated through the three-axis components of the accelerometer in the gravity field. Then, a reconstruction model of the terrain and strata deformation was proposed based on the rotation matrix and the arc model. To evaluate the monitoring system and validate the reconstruction model, a field experiment was conducted on a tidal flat in Changzhi Island for one week. The deformation of the terrain and strata and the pore water pressure were measured and obtained. The results demonstrate the feasibility of the proposed system.

Index Terms—Deformation reconstruction model, micro-electromechanical system (MEMS) sensor network (SN), terrain and strata deformation monitoring, tidal flat experiment.

I. INTRODUCTION

Gas hydrates are ice-like crystalline compounds comprised of water and methane gas, which form within sediments under low temperature and high pressure for certain gases [1], [2]. Gas hydrate is widely distributed, with large

Manuscript received 12 July 2022; revised 17 October 2022; accepted 21 October 2022. Date of publication 7 November 2022; date of current version 11 November 2022. This work was supported in part by the National Natural Science Foundation of China under Grant 41976055 and Grant 42106205, in part by the Finance Science and Technology Project of Hainan Province under Grant ZDKJ202019, in part by the Key Research and Development Project of Zhejiang Province under Grant 2020C03G2012430, and in part by Guangdong Basic and Applied Basic Research Foundation under Grant 2021A1515011475. The Associate Editor coordinating the review process was Nuria Novas. (*Corresponding author: Jiawang Chen*)

Yongqiang Ge, Chen Cao, Peng Zhou, Hai Zhu, and Qixiao Zhou are with the Ocean College, Zhejiang University, Zhoushan 316021, China (e-mail: ge_yongqiang@zju.edu.cn; cc666@zju.edu.cn; zp2010_ok@126.com; 12034056@zju.edu.cn; 3180100572@zju.edu.cn).

Jiawang Chen is with the Ocean College, Zhejiang University, Zhoushan 316021, China, also with the Hainan Institute, Zhejiang University, Sanya 572025, China, and also with the Engineering Research Center of Oceanic Sensing Technology and Equipment, Ministry of Education, Zhoushan 316021, China (e-mail: arwang@zju.edu.cn).

Chunying Xu is with the College of Engineering, Shantou University, Shantou 515063, China (e-mail: chunyingxu@stu.edu.cn).

Digital Object Identifier 10.1109/TIM.2022.3218336

reservoirs in the ocean, exhibits a high energy density, and is pollution-free, which is expected to be the ideal energy in the twenty-first century [3], [4]. However, gas hydrate trial production (i.e., mining) is still in the process of technical verification, and there are numerous technical difficulties and safety challenges that need to be resolved urgently, especially the in situ monitoring method of gas hydrate mining environments [5].

The South China Sea (SCS) is rich in gas hydrate resources. In May 2017 and March 2020, two small-scale trial productions were successfully carried out in the northern SCS [6]. These trial productions occurred in areas with flat seabed to avoid the potential risk of submarine landslides. In fact, most of the gas hydrates in the SCS are stored below sloped seabed, where the strength of the soil is low and easily damaged by disturbances [7], [8]. The mining process of gas hydrate is associated with the decomposition of gas hydrate, the weakening of cementation, and the migration of water and free gas. This may lead to the collapse of hydrate-bearing sediment and induce large-scale subsidence and sliding of the overlying seabed [9], thus potentially resulting in dramatic damage to seabed infrastructure and causing serious environmental and economic risk [5], [6].

Existing research reports on in situ long-term monitoring methods of seabed subsidence and slides in gas hydrate trial mining area remain sparse. For example, a servo-acceleration system [10] and a high-precision pressure gauge [11] were deployed to observe the seabed stabilities during the gas hydrate trial mining test in the Nankai Trough, Japan. A double-integral algorithm was used to calculate the seabed deformation, which may lead to a large accumulated error in long-term monitoring [12]. The pressure gauge measured the overlying water pressure, and the changes of the pressure serve as a proxy for seabed deformation. However, pressure gauges based on quartz strain undergo drift, accumulating further long-term monitoring errors [5]. In addition, horizontal deformation cannot be measured by pressure gauges. Moreover, both methods can only measure a single spatial position [13], [14].

The above problems apply to both monitoring deep-sea environments and shallow-water environments, like landslides. In the case of the latter, the technology of the micro-electromechanical system (MEMS) has been greatly developed in the last decade to overcome monitoring issues. MEMS sensors have the advantages of small size, lightweight, and low

power consumption and cost [15]. The MEMS sensor technology (i.e., MEMS inclinometer and MEMS accelerometer) has been applied to the geological deformation measurement. The feasibility and reliability of early warning systems based on MEMS tilt sensors and volumetric water content sensors have been proven through their successful application in landslide monitoring in many landslide sites in China and Japan [16]. In addition, MEMS accelerometers and MEMS gyroscopes are considered to be well-suited for terrain and landslide monitoring, and have been successfully used in laboratory tests [13], [15].

Bennett et al. [17] evaluated the performance of 3-D MEMS based on an in-place inclinometer–accelerometer array for monitoring the settling and lateral spreading of a soft clay deposit. The collected data were successfully compared to data measured with a state-of-the-practice instrument, supporting the use of the developed instrument in geotechnical applications.

In addition to overland monitoring systems, a new submarine landslide monitoring (SLM) system has recently been designed and tested [14]. Unlike the pressure gauges-based systems discussed above, it can monitor seabed deformation at different depths. Since it requires people (divers) to operate, it cannot be deployed in deep-sea environments. Moreover, the SLM system can only monitor the horizontal displacement of the strata, but not the deformation of the seabed terrain and strata simultaneously.

Measurand Company, Hanwell, NB, Canada, manufactured the MEMS accelerometer array, which is called Shape-Accel-Array (SAA). The SAA can measure the spatial shape of targets and is currently widely used in tunnel deformation, foundation subsidence, landslides and river delta, etc. [17], [18], as well as for the SLM [14]. However, it cannot be used in the deep sea and its deployment in engineering is difficult. For example, the SAA needs to be installed vertically in a polyvinyl chloride (PVC) pipe [19], and then, this pipe needs to be placed into a predrilled vertical borehole, and finally, soil needs to be filled into the pipe [20].

Here, a monitoring method based on a MEMS sensor network (SN) is proposed. Unlike previous methods, it can be deployed in the deep sea to monitor terrain and strata deformation in gas hydrate mining. It uses the inertial measurement unit (IMU) technology, which has previously been successfully applied in ground and landslide deformation monitoring [17], [19], [21]. The proposed monitoring system includes the multiple horizontal arrays (HAs) and vertical arrays (VAs), which can monitor the deformation of the seabed terrain and strata simultaneously. It also overcomes the problem [22] of synchronous acquisition and storage of multinode MEMS sensors in MEMS SN. Furthermore, the flexible HAs can be deployed in a large area on the seabed. The difficulty of deploying the VA was also reduced. It can be directly placed into the seabed without predrilling borehole.

The remainder of this article is organized as follows. Section II describes the concept and structure of the monitoring system. Section III presents the calculation principle of tilt angle and terrain and strata deformation. In Section IV, a field test was conducted for a tidal flat in Changzhi Island

to validate the performance of the monitoring system. Finally, Sections V and VI present discussions and conclusions, respectively.

II. MONITORING SYSTEM ARCHITECTURE

The monitoring system includes data acquisition and control system and the sensor monitoring network, as shown in Fig. 1. Among them, the data acquisition and control system can realize the time synchronization of all sensors in the SN, control the data acquisition and transmission, and preprocess the raw data. The SN includes terrain and strata deformation monitoring arrays, and each array has multiple monitoring nodes. It can monitor terrain and strata deformation simultaneously. After the monitoring is completed, the host computer is used to analyze and process the collected data, and plot the terrain and strata deformation curves.

The data acquisition and control system includes a power management module, a data acquisition module, and a system control module. The operating frequency of the system is adjustable, which is up to 1 Hz. In this article, the acquisition frequency is set to be 1/3600 Hz. The battery supplies power to the system control module with a voltage of 12 V and records the current value during operation. The power management module can discriminate abnormal conditions and automatically cut off the connection between the battery and the control module to avoid damage to the entire system.

Due to the large range of the target area and the large number of sensor arrays, a single data acquisition module is difficult to complete the synchronous acquisition of multiple sensor arrays. Thus, separate acquisition modules are configured to each sensor array. However, there is a time shift between different acquisition boards, and the shift will gradually increase as the operation period becomes longer due to the physical difference of the crystal oscillator. The relays are used in the system control module, which are turned ON and OFF simultaneously and periodically to achieve the synchronous control of different acquisition modulus.

Moreover, in order to improve the efficiency and stability of data acquisition and control system, a communication method based on RS485 bus is designed, which is widely used in industrial data communication and monitor-control system [23], [24]. RS485 adopts the master-slaver communication mode (Modbus communication protocol), and one master can be connected with multiple slaves. When the communication rate is lower than 100 kb/s, the longest communication distance and the maximum connected units can reach 1200 m and 32 units, respectively [24]. Therefore, the monitoring network containing multiple MEMS sensor nodes can be designed through RS485 bus, in which the control module is the primary host, and the acquisition module is both the primary slaver and secondary host. The primary host (control module) can perform time synchronization and power control for each slaver (acquisition module), and periodically turn ON and OFF the monitoring system and reduce power consumption. As for the secondary host (acquisition module), MEMS sensors are the secondary slavers. The acquisition module inquires all sensors through RS485 physical address in turn, and collects and stores the data in the SD card. Moreover,

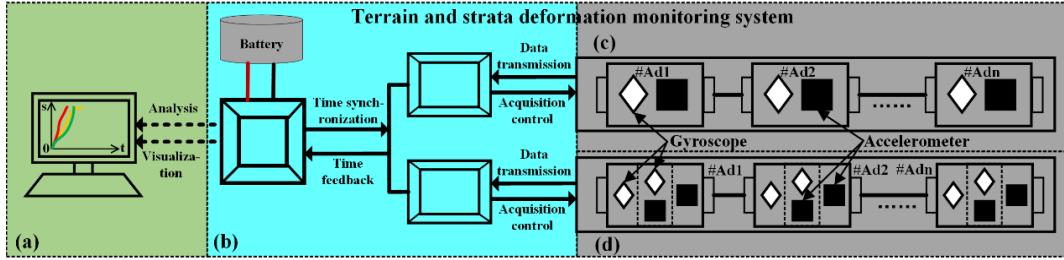


Fig. 1. (a) Host computer. (b) Data acquisition and control system. (c) Terrain deformation monitoring array. (d) Strata deformation monitoring array.

TABLE I
CHARACTERISTICS OF THE HA AND VA

Parameters	Length	Diameter	Number of nodes	Interval of nodes	Power consumption	direction
HA	20 m	44 mm	21	100 cm	4.20 W	Single-axis
VA	2 m	50 mm	5	40 cm	4.08 W	Dual-axis

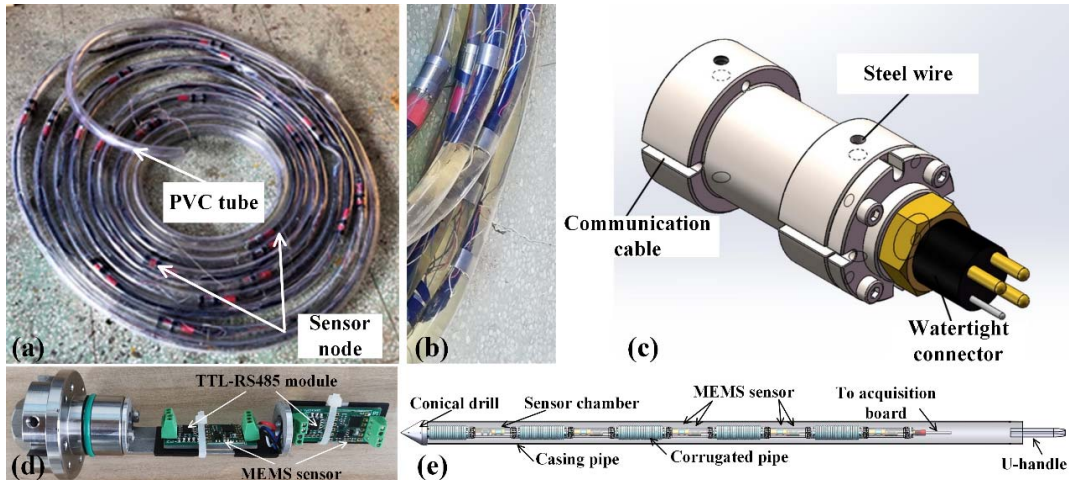


Fig. 2. (a) HA. (b) Oil filled tube. (c) Sensor node. (d) Structure of the sensor node of VA. (e) VA.

even if a sensor node fails, it will not affect the operation of the SN.

The SN includes terrain deformation monitoring array (HA) and strata deformation monitoring array (VA), and the characteristics of them are shown in Table I. The arrangement (i.e., the numbers and distances of sensors) of the MEMS sensors in the HA and VA is based on the sensor placement strategy with 2-D equal arc length nonuniform sampling [25], [26], and the terrain deformation of the experimental area can be successfully reconstructed. As shown in Fig. 2(a)–(c), the HA is inside the flexible PVC tube, which can ensure the relative spatial position of the sensors and strengthen the coupling effects with surrounding sediments. To prevent the HA from leaving the seabed due to its buoyancy, resulting in monitoring failures, the PVC tube is filled with oil, and the lead blocks are placed between adjacent sensors to increase the overall density of the HA. The length of HA is 21 m, with 21 sensors, and the interval between adjacent sensors is 1 m.

As shown in Fig. 2(d), the VA consists of the auxiliary deployment part and the monitoring part. As shown in Table I, the VA has a length of 2 m and a diameter of 50 mm, in which the length of U-shaped handle, monitoring part,

and conical drill is 300, 1600, and 100 mm, respectively. The auxiliary deployment part can deploy the monitoring part inside the strata, which includes conical drill, stainless steel casing pipe, plug, and U-handle. As shown in Fig. 2(e), the U-shaped handle is on the stainless steel casing pipe and used to cooperate with remotely operated vehicle's (ROV) manipulators to recover the casing pipe after the VA is successfully placed. The conical drill is connected to the internal sensor array to reduce resistance during deployment process and ensure the VA penetrates vertically into the strata.

The monitoring part is mainly composed of MEMS sensors, sensor chambers, corrugated pipes, and watertight cables. Totally, there are five monitoring nodes, with an interval of 40 cm. Each monitoring node contains two mutually perpendicular MEMS sensors. The sensors are placed in the sensor chamber and communicate with data acquisition and control system through watertight cables to achieve cascading and communication on the deep seabed. The corrugated pipe connects the adjacent sensor chambers, can be regarded as a soft joint, and will bend and twist when the sediment slides or deforms.

TABLE II
SPECIFICATIONS OF SIX-AXIS MEMS SENSOR

Size	15.24 mm × 15.24 mm × 2 mm
Measurement range	Accelerometer: ±2 g Gyroscope: ± 250°/s
Resolution	Accelerometer: ±6.1 × 10 ⁻⁵ g Gyroscope: ± 0.0076 °/s
Stability	Acceleration: 0.01 g Angle: 0.01 °
Operation voltage	3.3-5 V
Baud rate	115200

The deployment processes of the VA are as follows: 1) the VA is penetrated into the seabed segment by segment with the assistance of ROV's manipulator; 2) after penetrating to a specific depth, the plug is pull out, and the casing pipe is separated from the conical drill; and 3) finally, the ROV's manipulator holds the U-handle and pulls out the casing pipe, leaving the monitoring part in the strata to conduct monitoring tasks.

The MEMS sensor used in this article is called JY61P (Weite Intelligent and Technology Company, Shenzhen, China), which consists a three-axis accelerometer and a three-axis gyroscope. The MEMS sensor is with high-performance microprocessor, advanced dynamic attitude solution method, and Kalman filtering algorithm. It can efficiently calculate the current attitude, reduce the measurement noise, and improve the measurement accuracy [5]. The characteristics of the MEMS sensor are shown in Table II. A TTL-RS485 module is equipped with each sensor nodes in order to cascade all MEMS sensor nodes and establish communication with the data acquisition and control system, as shown in Fig. 2(d). The MEMS sensors on SN have unique physical address, and data acquisition modulus inquire and collect the data of them in turn. In addition, in order to ensure the operation of MEMS sensors in deep sea, sensor chambers are designed to protect the MEMS sensors from high pressure and the communications between sensors and data acquisition modulus through watertight connectors, as shown in Fig. 2(c).

III. DEFORMATION MEASUREMENT PRINCIPLE

A. Monitoring Principle of the Tilt Angle

The deformation and displacement of the terrain and strata are related to the geodetic coordinate system, and a relatively fixed reference system should be established [27]. The gravitational field and geomagnetic field are two physical references commonly used in measurement. Compared with the gravitational field, the strength of the geomagnetic field is weak and easily affected by the surrounding environment [15]. Therefore, the MEMS accelerometer is more widely used in the deformation monitoring of geological engineering.

Assuming that $r(e_x, e_y, e_z)^T$ is a fixed reference in space, where at least one of the e_x, e_y, e_z is not equal to zero. Establishing a Cartesian reference coordinate system ($X-Y-Z$), which coincides with the sensitive axis ($x-y-z$) of the vector r .

When the coordinate system $x-y-z$ of a certain unit is rotated according to the rotation matrix C in the Cartesian coordinate system, the initial state of a certain measurable physical quantity is S , and S can be expressed as

$$S = \begin{bmatrix} S_x \\ S_y \\ S_z \end{bmatrix} = C \begin{bmatrix} e_x \\ e_y \\ e_z \end{bmatrix} + a \quad (1)$$

where a and C are the translation and pure rotation of the reference, respectively.

A fixed and nonzero vector r is constructed, and the physical quantity S is measured after the unit is rotated to measure the spatial attitude of the unit, that is, the rotation matrix C . The dimensions of the matrix are determined by the physical quantities that can be measured and to be measured. When one of the axes is not equal to 0, the rotation angle around the other two axes can be obtained. As long as any two axes of r are not equal to 0, the measurement requirement of spatial attitude can be met. Only the vertical deformation changes are considered in terrain deformation measurement, so each monitoring node of the HA only needs one single-axis sensor, while two mutually perpendicular sensors are required to form a monitoring node in strata deformation measurement.

In the gravitational field, the gravitational acceleration is an ideal reference vector. When the sensitive axis of the accelerometer is in nonvertical state, a gravitational acceleration component will be generated on the sensitive axes of accelerometer. The tilt angle of the accelerometer can be obtained by measuring the gravitational components. Assuming that the sensitive axis ($X-Y-Z$) of the accelerometer coincides with the system coordinate ($x-y-z$) in the initial state, and then, the measurement value of the three-axis accelerometer can be expressed as

$$A = \begin{bmatrix} A_x \\ A_y \\ A_z \end{bmatrix} = C \begin{bmatrix} 0 \\ 0 \\ g \end{bmatrix} + a \quad (2)$$

where A_x, A_y , and A_z are the measured acceleration in x -, y -, and z -axes, respectively, C is the rotation matrix, $[0, 0, g]^T$ is the gravitational acceleration in initial state, and a is the linear acceleration. The linear acceleration of terrain and strata deformation can be ignored because it is much smaller compared with the gravitational acceleration.

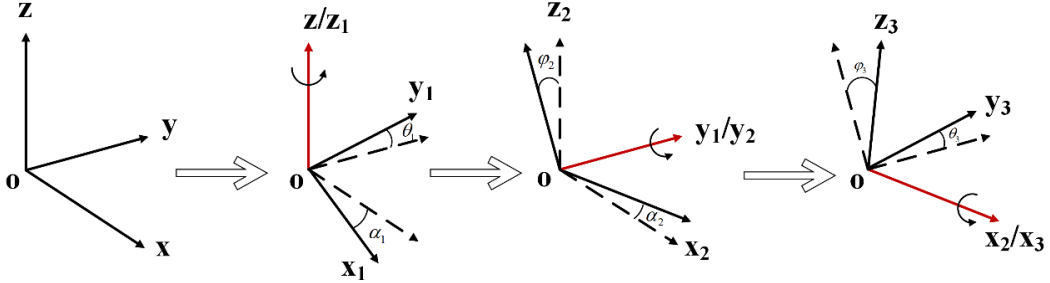


Fig. 3. Rotation angle and rotation matrix of the sensor.

As shown in Fig. 3, in the calculation of the rotation matrix, the monitoring unit rotates an angle of φ (yaw angle), θ (pitch angle), and α (roll angle) around $z-y-x$ -axis of the initial coordinate system ($o-x-y-z$), respectively, and the rotated coordinate system is $o_s-x_s-y_s-z_s$. The rotation matrix after each coordinate system rotation can be expressed as [5]

$$C_z(\varphi) = \begin{bmatrix} \cos\varphi & \sin\varphi & 0 \\ \sin\varphi & \cos\varphi & 0 \\ 0 & 0 & 1 \end{bmatrix} \quad (3)$$

$$C_y(\theta) = \begin{bmatrix} \cos\theta & 0 & -\sin\theta \\ 0 & 1 & 0 \\ \sin\theta & 0 & \cos\theta \end{bmatrix} \quad (4)$$

$$C_x(\alpha) = \begin{bmatrix} 1 & 0 & 0 \\ 0 & \cos\alpha & \sin\alpha \\ 0 & -\sin\alpha & \cos\alpha \end{bmatrix}. \quad (5)$$

Therefore, the rotation matrix from initial coordinate system ($o-x-y-z$) to rotated coordinate system ($o_s-x_s-y_s-z_s$) can be expressed as

$$\begin{aligned} C &= C_x C_y C_z \\ &= \begin{bmatrix} 1 & 0 & 0 \\ 0 & c\alpha & s\alpha \\ 0 & -s\alpha & c\alpha \end{bmatrix} \begin{bmatrix} c\theta & 0 & -s\theta \\ 0 & 1 & 0 \\ s\theta & 0 & c\theta \end{bmatrix} \begin{bmatrix} c\varphi & s\varphi & 0 \\ s\varphi & c\varphi & 0 \\ 0 & 0 & 1 \end{bmatrix} \\ &= \begin{bmatrix} c\theta c\varphi & c\theta s\varphi & -s\theta \\ -s\varphi c\alpha + c\varphi s\alpha s\theta & c\varphi c\theta + s\theta s\alpha s\varphi & c\theta s\alpha \\ c\varphi s\theta c\alpha + s\varphi s\theta & -s\theta c\varphi + s\theta c\alpha s\varphi & c\alpha c\theta \end{bmatrix} \quad (6) \end{aligned}$$

where $c(*)$ and $s(*)$ represent $\cos(*)$ and $\sin(*)$.

The tilt angle of x - and y -axes can be obtained by combining (2) and (6), that is,

$$\begin{bmatrix} A_x \\ A_y \end{bmatrix} = \begin{bmatrix} -\sin\alpha \cdot \cos\theta \\ \sin\theta \end{bmatrix}. \quad (7)$$

Which is [28]

$$\begin{cases} \alpha = \arcsin\left(\frac{-A_y}{\cos\theta}\right) \\ \theta = \arcsin(A_x) \end{cases} \quad (8)$$

where α and θ are the tilt angle around x -axis (roll angle) and y -axis (pitch angle), respectively.

B. Reconstruction Principle of Terrain Deformation

Terrain deformation mainly includes the seabed subsidence and uplift. Accordingly, only the vertical changes of the HA are considered in the monitoring of terrain deformation, and

the 3-D terrain reconstruct can be simplified as the 2-D curve changes of the HA.

The HA is inside the oil-filled PVC pipe, and the initial yaw angle (around z -axis) of all sensor nodes is the same as the z -axis of the geodetic coordinate system. When reconstructing the shape of HA caused by terrain changes, the shape between the sensor node can be approximately regarded as an arc. For an arc, if the radius of the arc, the coordinates of the start point, and the center are known, the coordinates of the endpoint can be calculated. As shown in Fig. 4, the central angle of the arc $S_i S_{i+1}$ can be expressed as

$$\beta_i = \theta_{i+1} - \theta_i \quad (9)$$

where θ_i and θ_{i+1} are the pitch angle of the sensor S_i and sensor S_{i+1} , respectively. The radius of the arc is $r_i = l/\beta_i$ (l is the intervals of the adjacent sensor), and the coordinates of the center O_i in the coordinate system $O_i-X_i-Y_i-Z_i$ (sensor S_i as the origin) and the coordinates of the endpoint in the coordinate system $O_i-X_i-Y_i-Z_i$ can be expressed as [15]

$$\begin{aligned} S_{i+1}^i &= [dx, 0, dz]^T \\ &= \begin{cases} [r_i \sin \beta_i, 0, r_i - r_i \cos \beta_i]^T, & (\beta \neq 0) \\ [l, 0, 0]^T, & (\beta = 0). \end{cases} \quad (10) \end{aligned}$$

And the endpoint in the reference coordinate system $O-X-Y-Z$ can be expressed as

$$\begin{bmatrix} S_{i+1}^0 \\ 1 \end{bmatrix} = H_i^0 \begin{bmatrix} S_{i+1}^i \\ 1 \end{bmatrix} = \begin{bmatrix} C_i^0 & S_i^0 \\ O_3^T & 1 \end{bmatrix} \begin{bmatrix} S_{i+1}^i \\ 1 \end{bmatrix} \quad (11)$$

where C_i^0 is the rotation matrix from the reference coordinate system $O-X-Y-Z$ to the coordinate system $O_i-X_i-Y_i-Z_i$, which can be expressed as: $C_i^0 = C_{i-1}^0 C_i^{i-1}$.

To evaluating the reconstructed model in the following tidal flat experiment, a 3-D laser scanner is used to collect and scan the terrain of the monitoring area after the tide ebbs to compare with the terrain deformation changes and the reconstructed shape of the sensor array. The maximum root-mean-square error (RMSE), mean absolute error (MAE), and maximum error (ME) are used to quantitatively evaluate the reconstructed model.

C. Reconstruction Principle of Strata Deformation

As mentioned in Section II, each monitoring node of the VA contains two MEMS sensors whose initial yaw angles are perpendicular to each other. However, the initial yaw angle of the adjacent sensor is the same, which are designed to monitor

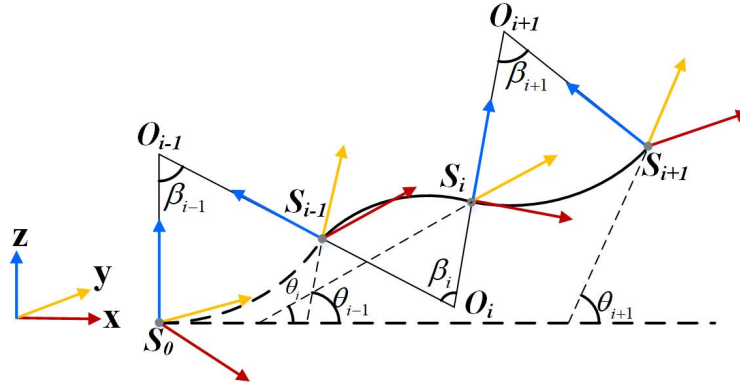


Fig. 4. Schematic of the arc model.

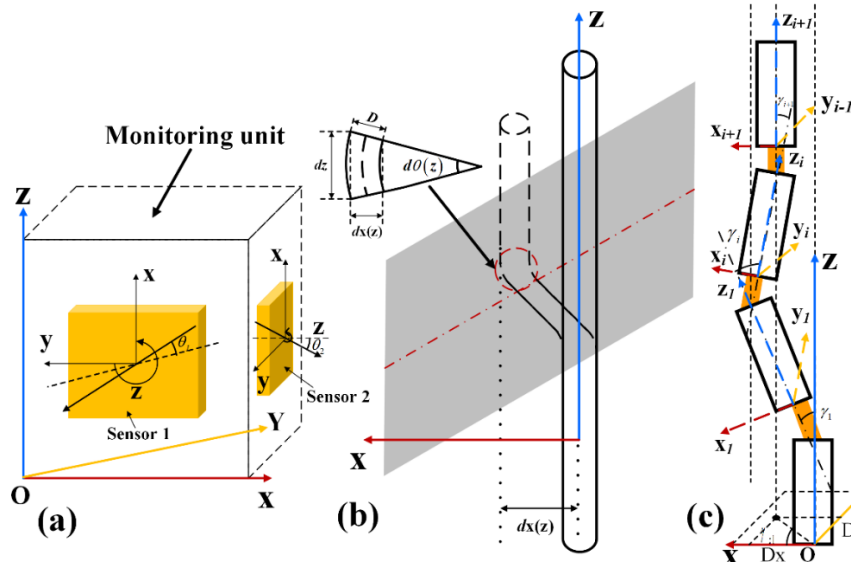


Fig. 5. Deformation monitoring principle and process of the strata. (a) MEMS sensor nodes on the monitoring unit. (b) Deformation of VA in X-Z plane. (c) Reconstruction principle of strata deformation.

the tilt angle and deformation of the strata in the direction of x - and y -axes.

As shown in Fig. 5, the processes to calculate the horizontal deformation of the strata are as follows: first, calculating the tilt angle of the sensors in the vertical plane according to the component of the gravitational acceleration on the sensitive axes of the MEMS accelerometer; then, calculating the tilt angle and inclination azimuth of the monitoring node in the geodetic reference coordinate system according to the tilt angle of the two sensors in the same monitoring node; and finally, taking the deepest monitoring node as the reference node, calculating the spatial coordinates of all monitoring nodes in turn based on the arc model, and solving the deformation curve and displacement of the VA.

As mentioned in Section III-A, the pitch angle of the sensors can be expressed as

$$\begin{cases} \theta_1 = \arcsin(g_{x1}/g) \\ \theta_2 = \arcsin(g_{x2}/g) \end{cases} \quad (12)$$

where θ_1 and θ_2 are the pitch angle of the sensors that in XZ plane and YZ plane, respectively. g_{x1} and g_{x2} are

the gravitational acceleration component of the corresponding sensor in x -axis.

The tilt angle γ_i of the monitoring node $\#i$ relative to the Z -axis (reference coordinate system) and the angle γ_{zi} between the projections line of the z -axis of the monitoring node on the XY plane and the X -axis can be expressed as [29]

$$\gamma_i = \arcsin\left(\cos\theta_2 \cdot \sqrt{1 - (\cos\theta_1/\cos\theta_2)^2}\right) \quad (13)$$

$$\gamma_{zi} = \arctan\left(\frac{\sin\theta_2}{\cos\theta_1} \sqrt{\cos^2\theta_2 - \cos^2\theta_1}\right). \quad (14)$$

The coordinates of the node $\#i$ in the coordinate system $O_{i-1}-X_{i-1}-Y_{i-1}-Z_{i-1}$ (node $\#i-1$ as the origin) can be expressed as

$$S_{i+1}^i = [l \cdot \sin \Delta\gamma_i \cdot \sin \gamma_{zi}, l \cdot \sin \Delta\gamma_i \cdot \cos \gamma_{zi}, l \cdot \cos \Delta\gamma_i] \quad (15)$$

where $\Delta\gamma_i$ is the tilt angle difference of the adjacent node, $\Delta\gamma_i = \gamma_i - \gamma_{i-1}$, and l is the interval of the adjacent node.



Fig. 6. (a) Location of Changzhi Island. (b) Field experimental area.

Thus, the coordinates of the node $\#i + 1$ in the reference coordinate system $O-X-Y-Z$, S_{i+1}^o can be expressed as

$$\begin{bmatrix} S_{i+1}^o \\ 1 \end{bmatrix} = H_i^o \begin{bmatrix} S_i^o \\ 1 \end{bmatrix} = \begin{bmatrix} R_i^o & S_i^o \\ O_3^T & 1 \end{bmatrix} \begin{bmatrix} S_{i+1}^o \\ 1 \end{bmatrix} \quad (16)$$

where R_i^o is the rotation matrix from the reference coordinate system $O-X-Y-Z$ to the coordinate system $O_i-X_i-Y_i-Z_i$ (node $\#i$ as the origin), which can be expressed as: $R_i^o = R_{i-1}^o R_i^{i-1}$. Rotating the coordinate system $O_i-X_i-Y_i-Z_i$ around the z -axis by $-\gamma_i$, the directions of the x -axis of the coordinate system $O_{i+1}-X_{i+1}-Y_{i+1}-Z_{i+1}$ and the rotated coordinate system $O'_i-X'_i-Y'_i-Z'_i$ are determined.

IV. IN SITU MONITORING EXPERIMENT AND RESULTS

A. Study Area

Changzhi Island ($122^{\circ}10'E$, $29^{\circ}58'N$) is located in the south of Zhoushan Island, Zhejiang, China, as shown in Fig. 6. The Changzhi Island is 7.3 km away from Dinghai district and 350 m away from Zhoushan Island. The coastline is 13.82 km long and covers the land area that is 6.30 km^2 . The experimental area is the north of Changzhi Island, as shown in Fig. 6. The natural experimental conditions on the Changzhi Island are very good. A large range of muddy tidal flat has been formed in Changzhi Island after several sea reclamations, contains thick soft sediment which has high water content and large initial void ratio, and is mainly flow plastic clay [30].

The tidal flat is a natural experimental site, and the terrain and strata of which undergo regular deformation under the action of periodic tides and waves [31]. Therefore, the tidal flat experiment can test the deformation monitoring performance of the MEMS SN. Due to the influences of tides, wave circulation, and erosion, the terrain and strata deformation of Changzhi Island's tidal flat are very complex. The water level of the formation will increase during high tide, which will lead to the increase of pore water pressure (PP) in the strata, and the reduction of effective stress and strength of the strata. The terrain deformation of the tidal flat in Changzhi Island includes sediment deposition or erosion, as well as soil consolidation and expansion, while the strata deformation includes soil sliding or flow due to liquefied failure and shear failure. However, research on terrain and strata deformation in tidal flat on the Changzhi Island has never been reported before.

B. Monitoring Experiment

Fig. 7 shows a schematic of the terrain and strata monitoring of the tidal flat, and Fig. 8 presents a diagram of the

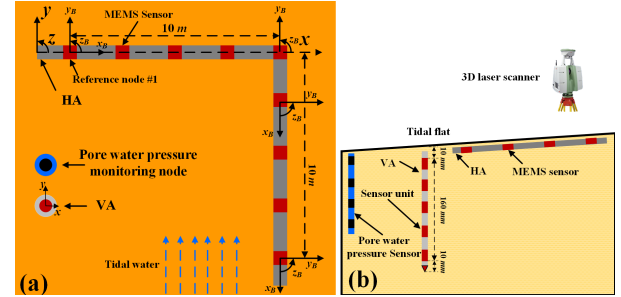


Fig. 7. Schematic of the experimental setup. (a) Top view of tidal flat. (b) Side view of tidal flat.



Fig. 8. Deployment of the MEMS SN: (a) HA and (b) and (c) VA.

deployment of the SN. The length of the HA is 20 m, with 20 monitoring nodes, and the interval of the nodes is 1 m, as mentioned in Section II. The HA is equally divided into two sections (each section is 10 m), arranged in an "L-shaped" to a depth of 10 cm of the tidal flat. The VA is deployed at a depth of 1.8 m inside the strata, and the highest and lowest monitoring nodes are 10 and 170 cm deep from the surface of the tidal flat, respectively. In addition, an array composed of four PP sensors was arranged around the SN, and the measuring range and the accuracy level are 0–30 kPa and 0.5% FS, respectively. The PP sensor used in this article is called SCYG318 (SEN Measurement and Control Technology Company Ltd., Wuxi, China).

All the sensors on the SN, including HAs and VAs, are synchronously collected and saved by the data acquisition and control system. The data collection frequency is set to 1/3600 Hz (that is once per hour), and ten groups of data of every node will be collected each hour. The averaged of the data are taken as the data of monitoring nodes at the current moment after the collected data are preprocessed and the abnormal data are deleted. Then, the deformation curve of the sensor array is reconstructed using the terrain and strata deformation reconstruction method, as mentioned in Section III. The terrain deformation changes, and the reconstructed shape of the sensor array could be compared with the data from the 3-D laser scanner, which can collect data after the tide ebbed and scans the terrain of the monitoring area once a day.

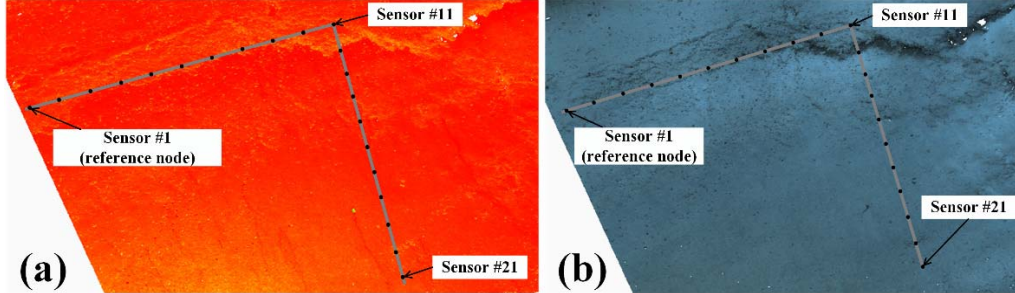


Fig. 9. Study area obtained from 3-D scanner: (a) intensity map and (b) texture map.

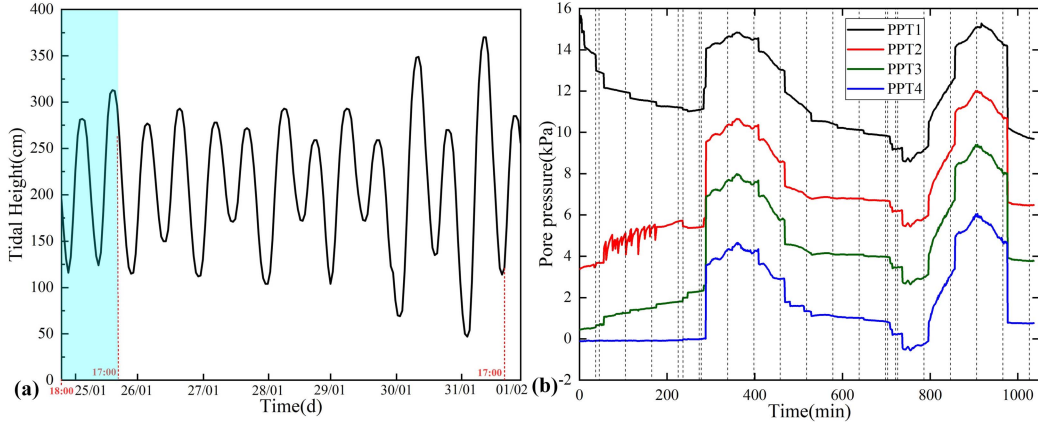


Fig. 10. Tide height and PP: (a) tide height during the field experiment, and the blue rectangular is the data from 18:00 on January 24 to 17:00 on January 25 and (b) PP corresponding to the blue rectangular in the left figure, and the data in every hour are separated by the dotted line.

Fig. 9 shows the study area obtained from the commercial software of the Cyclone.

C. Experimental Results

The SN was deployed from January 24, 2022 to January 31, 2022. The HA was operated from 18:00 on January 24 to 17:00 on January 31, and the VA was operated from 10:00 on January 25 to 8:00 on January 30.

1) Tide Height and PP: Fig. 10(b) shows the PP from 17:00 on January 24 to 17:00 on January 25. Due to the failure of the data acquisition module, part of the PP data is missing and discontinuous. Also, the amount of recorded data is not the same, so the data in every hour are separated by a dotted, as shown in Fig. 10(b). Sensor #4 was located on the surface of the tidal flat, and the PP was recorded between 0:00 and 1:00 on January 25, indicating that the tide began to rise above the measuring hole during this time. The corresponding tide level increased from 226 to 264 cm during this period, i.e., about 38-cm increment. The changes of the recorded PP were about 4.28 kPa, which was approximately equivalent to a height of 43.7 cm when converted into water depth. The excess pressure may be related to wave height at high tide and the slope of the tidal flat.

Fig. 10(a) shows the tide height of the Changzhi Island, Dinghai district, which is obtained from the National Marine Data Information Center, Tianjin, China. The time when the tidal water touches the SN in the study area and the corresponding tide height can be estimated from the changes of the PP, and the tide height table obtained from the National Marine Data Information Center. The height difference between the

measuring hole of VA and PP sensor array is about 10 cm. Thus, the VA begins to be submerged by tidal water when the tide height reaches 215 cm. On the other hand, the HA is longer and has a larger span. When tidal water first reaches the lowest node #21 and the whole HA is submerged, the tide height is 210 and 230 cm, respectively.

2) Changes of Tilt Angle of the Sensors on HA: Fig. 11 shows the relationships of the pitch angle of the sensors (#1 and #11) and the tide height. The pitch angle is calculated as mentioned in Section III-A. It is hard to accurately monitor the pitch angle changes of the sensors during the high tide and ebb due to the limitation of collection frequency, but the cumulative changes can be obtained.

As shown in Fig. 11, the pitch angle change of reference node is small, without cumulative angle changes, but a small range of vibration occurred. However, the change period of the pitch angle of sensor #11 has exhibited an obvious periodicity which is almost the same as that of the tidal water, showing an obvious periodicity. The pitch angle becomes larger at high tide and smaller at low tide. The tide is semidiurnal in Dinghai district (Zhoushan, Zhejiang Province) with two high tides and two low tides every 24 h [32]. Similarly, the variation of the pitch angle also has two maxima and two minima. In addition, the pitch angle of sensor #11 decreased gradually, which decreased by 0.154° during the monitoring period, with the maximum pitch angle of 0.053° and the minimum pitch angle of -0.222° . The changes of pitch angle of all sensors on HA are shown in Table III, where the final maximum pitch angle is 0.087° (sensor #20) and the final minimum pitch angle is -0.344° (sensor #8).

TABLE III
PITCH ANGLE OF ALL SENSORS ON THE HA

Sensor	Max.ang ¹ (°)	Min.ang ² (°)	Mean.ang ³ (°)	Fin.ang ⁴ (°)
1	0.029	-0.073	-0.012	-0.059
2	0.081	-0.080	-0.006	0.027
3	0.047	-0.172	-0.066	-0.110
4	0.042	-0.206	-0.080	-0.172
5	0.095	-0.029	0.031	0.067
6	0.072	-0.042	0.019	0.043
7	0.065	-0.016	0.021	0.038
8	0.111	-0.441	-0.178	-0.344
9	0.057	-0.035	0.012	0.001
10	0.052	-0.057	-0.011	-0.001
11	0.053	-0.222	-0.079	-0.155
12	0.031	-0.029	0.006	-0.014
13	0.016	-0.041	-0.014	0.015
14	0.070	-0.001	0.031	0.056
15	0.092	-0.007	0.036	0.074
16	0.049	-0.048	0.006	0.028
17	0.071	-0.015	0.025	0.057
18	0.014	-0.121	-0.053	-0.065
19	0.042	-0.044	-0.006	0.013
20	0.136	-0.033	0.066	0.087
21	0.002	-0.416	-0.286	-0.342

¹ Max.ang: maximum angle. ² Min.ang: minimum angle. ³ Mean.ang: mean angle. ⁴ Fin.ang: final angle.

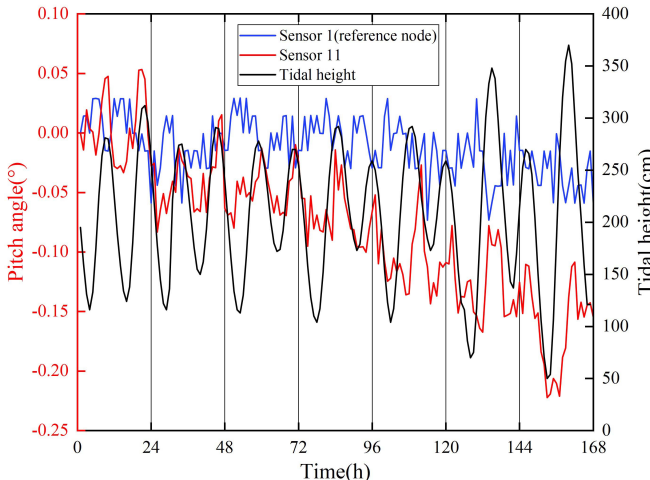


Fig. 11. Pitch angle of the reference sensor #1 and sensor #11.

3) *Changes of Deformation Curve of the HA*: Fig. 12(a) shows the shape changes of the HA every 3 h with sensor #1 as the reference node. Fig. 12(b) shows the vertical deformation changes of the sensor #11 and sensor #21, which have strong synchronization, increasing and decreasing almost at the same time, but the change rate and magnitude are different.

There is a significant phase difference between the vertical changes of sensor #11 and the tide height, as shown in Fig. 13. The uplift deformation of sensor array is not due to the buoyancy of sea water and the impact of tide and wave since the lifting is not synchronized with high tide. The soils in the tidal flat are subjected to cyclic loads of tide water. When the tide height is higher than the surface of tidal flat, the seabed

is completely submerged by the tide water. While during the tide water bulge or ebb, the seabed is sometimes submerged and sometimes exposed to the air. And when the tide height is lower than the surface of tidal flat, the seabed is completely exposed to the air. As shown in Fig. 14, the maximum water depth appears at the wave crest (at highest tide level) and element 1 endures the maximum vertical compressive stress σ'_{\max} . The minimum vertical compressive stress σ'_{\min} acts on element 3 when the minimum water depth appears at the wave trough (at lowest tide level). As for tide flat, the minimum vertical compressive stress is equal to zero when the tide flat exposed to the air.

Since the permeability of the seabed soil is pretty small during each tide water cycle and can be ignored, the tide flat surface is assumed to be undrained, and the tide wave-induced dynamic pressure P can be applied on the tide flat surface as a total stress. Based on the linear wave theory, P is given as [33]

$$p = \frac{\gamma_w H}{2 \cosh(kh)} \sin(kx - \omega t) \quad (17)$$

where γ_w is the unit weight of seawater, H is the wave height, k is the wavenumber, h is the water depth, ω is the angular frequency, x is the horizontal ordinate, and t is the time.

According to the principle of effective stress, if the seabed soil is compressed so rapidly that there is no time to drain out the pore water during tide water bulge, the pore water may exceed the hydrostatic pressure and the increment is excess pore water pressure (EPP), and the change of soil volume (the volumetric strain) is the essence of EPP [34]. The volumetric

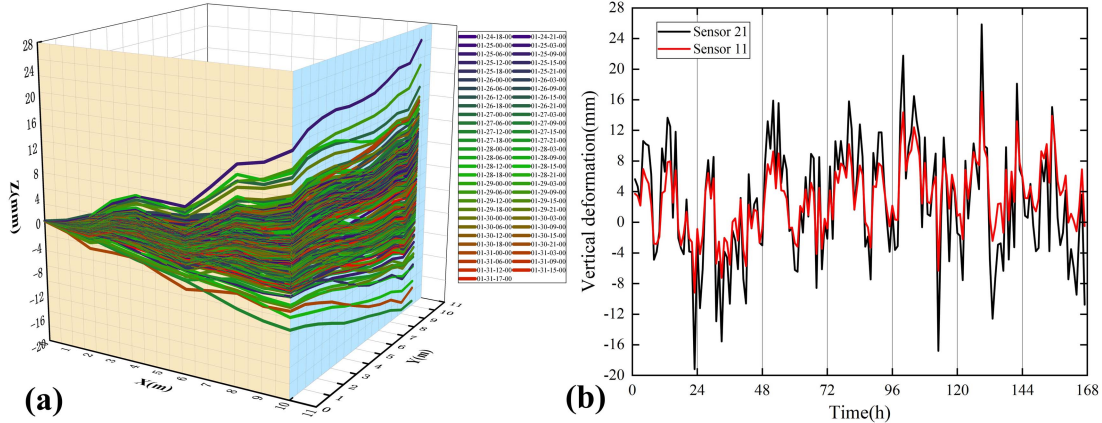


Fig. 12. (a) Deformation shape of the HA in every three hours. (b) Vertical changes of the sensors #11 and #21.

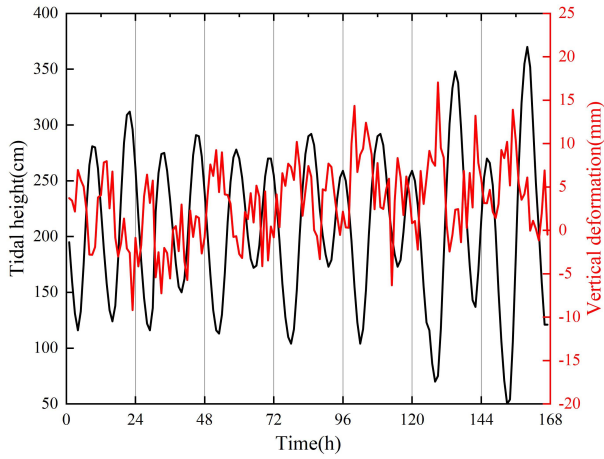


Fig. 13. Tide height and the vertical changes of sensor #11.

strain due to tide wave loads is described as [35]

$$\varepsilon = -np/\beta \quad (18)$$

where n is the soil porosity, p is the excess pore pressure, and β is the bulk modulus of water. ε can be expressed as

$$\varepsilon = \varepsilon_e + \varepsilon_p \quad (19)$$

where ε_e and ε_p stand for the elastic and plastic volumetric strains, respectively. The total external σ_{tot} can be expressed as

$$\sigma_{\text{tot}} = \sigma + \tau. \quad (20)$$

The volumetric strains coinciding with the volume change ΔV (change between the initial state and the momentary state) of the seabed soil in one cycle of tidal wave are shown in Fig. 14. If compressive stresses are supposed to be positive, the maximum positive EPP corresponding to the maximum compressive volumetric strain [as shown in (18)] appears under the wave crest (element 1 in Fig. 14) with maximum compressive stress. Similarly, the maximum negative EPP coinciding with the maximum expansion volumetric strain appears under the wave trough with minimum compressive stress (element 3 in Fig. 14). The total stress can be divided into the spherical stress (the compressive stress acting on elements 1 and 3 in Fig. 14) and the deviatoric stress (the

compressive stress acting on elements 2 and 4 in Fig. 14) according to (20).

The volumetric strain caused by external loads can be divided into elastic strain and plastic strain based on the elastoplastic theory [as shown in (19)]. The elastic strain is recoverable during each tide cycle ($\Delta V_{e1} = -\Delta V_{e3}$), but the plastic strain is irrecoverable in each cycle ($\Delta V_{p1} \neq \Delta V_{p3}$). No volumetric strain ($\Delta V_2 = \Delta V_4 = 0$) is caused by the shear stress. Thus, the plastic compressive volumetric strain accumulates during each cycle ($V_1 + V_2 + V_3 + V_4 > 0$), which proves the cyclic tide wave-induced vertical changes of the tidal flat surface, as shown in Table IV. Similar experimental phenomena were also observed [36], [37], [38].

Since sensor #21 located at the lowest position and submerged by the tide with the longest time, the averaged affected time by the tide and wave is the longest, and the relative vertical changes of sensor #21 are also the largest. The maximum uplift and subsidence of sensor #21 are 25.85 and 19.19 mm, respectively. Moreover, the vertical change rate (per hour) of sensor #21 is also the largest, and the maximum uplift rate and subsidence rate of whom are 21.53 and 25.77 mm/h, respectively. The average vertical change of sensor #21 is a lift of 2.54 mm during a week of continuous monitoring. As shown in Table IV, the mean vertical changes of all sensors are positive, and the terrain generally presents the uplift trend, which is consistence with the phenomenon of long-term silt accumulation in the study area.

Fig. 15 shows the deformation curves obtained by the HA and the 3-D laser scanner at different times from January 25 to January 31. The 3-D laser scanner can only collect the coordinates of the study area when it is exposed. The data in Fig. 15 and Tables V and VI are in the respect to the reference node and the initial position. That is, they are the relative coordinates with respect to those in the initial position. The coordinates of the reference node of the HA are calibrated and corrected with the precise coordinates obtained by the 3-D laser scanner. According to Fig. 15 and Tables V and VI, the overall changes in the coordinates of the tidal obtained from the HA and the 3-D laser scanner are almost consistent. Table VII shows the deformation errors between the HA and 3-D laser scanner. The data obtained by the HA differed slightly from those collected by the 3-D laser scanner, with a

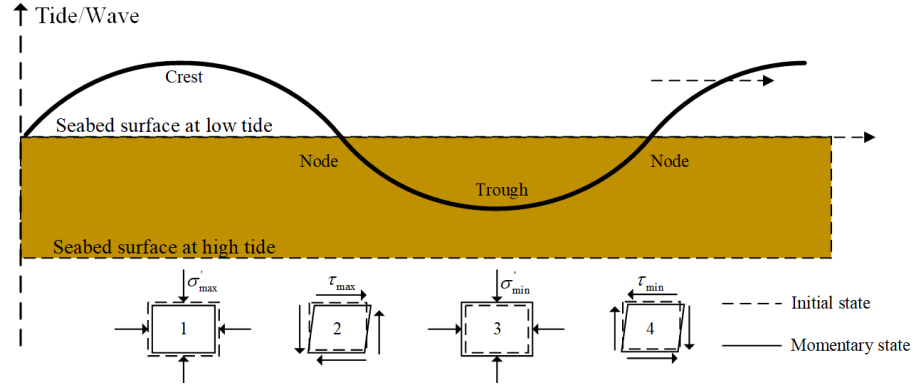


Fig. 14. Wave/tide-induced stress in seabed (brown rectangle represents the relative position changes of the surface of the tidal flat relative to the tide height), modified from [38].

TABLE IV
VERTICAL CHANGES OF ALL SENSORS ON THE HA

Sensor	Max.def ⁵ (mm)	Min.def ⁶ (mm)	Max.def.ph ⁷ (mm)	Min.def.ph ⁸ (mm)	Mean.def ⁹ (mm)
1	0	0	0	0	0
2	0.84	-1.11	0.63	-1.12	-0.06
3	2.34	-3.00	2.26	-3.73	0.36
4	5.23	-2.96	3.78	-5.65	1.42
5	6.75	-3.37	4.77	-6.70	1.63
6	6.55	-4.82	5.88	-7.96	0.97
7	6.35	-6.34	7.01	-9.25	0.41
8	10.02	-6.32	7.39	-9.93	1.58
9	13.97	-7.69	8.41	-10.47	2.82
10	14.82	-8.66	9.42	-11.36	2.61
11	17.05	-9.18	10.56	-12.27	3.19
12	19.01	-10.10	11.67	-13.54	3.61
13	19.86	-11.28	12.68	-14.92	3.47
14	20.21	-12.69	13.56	-16.20	3.11
15	19.87	-14.18	14.43	-17.53	2.31
16	19.97	-15.17	15.55	-19.10	1.73
17	20.27	-16.05	16.87	-20.62	1.23
18	21.34	-17.07	18.13	-21.89	1.26
19	22.65	-17.97	19.26	-23.28	1.56
20	22.76	-19.36	20.51	-24.53	0.82
21	25.85	-19.19	21.53	-25.77	2.54

⁵ Max.def: maximum deformation; ⁶ Min.def: minimum deformation; ⁷ Max.def.ph: maximum deformation in one hour; ⁸ Min.def.ph: minimum deformation in one hour; ⁹ Fin.def: final deformation.

maximum absolute error of 4.94 mm. The maximum RMSE, MAE, and ME are 3.04, 2.82, and 4.94 mm, respectively.

4) *Changes of Pitch Angle of the Sensors on VA:* Fig. 16(a) shows the pitch angle of all sensors on VA. Sensor #1 and sensor #2 are located in 10 cm deep from the surface of the tidal flat, and the pitch angle of them changed obviously compared with other sensors. Data of Sensor #1 and sensor #2 show five obvious sudden inclinations. The first one occur in T0 moment, sensor #1 and sensor #2 slightly tilt in the positive direction, and the pitch angles are 0.237° and 0.292°. After that, the sensors recover and tilt to -0.2° in the negative direction and keep it until T1 moment. At the beginning of T1, the pitch angle reaches -0.3°. Then, sensor #1 suddenly tilts greatly, and the pitch angle reaches -0.98°. However, it immediately recovers to about -0.3°, resulting in a cumulative pitch angle of -0.1° in T1 moment, and keep it until T4 moment.

The similar situation also occurs in T2 and T3 moments, where the pitch angles of sensor 1 and sensor 2 reach -1.018° and -1.511°, respectively. However, they recover quickly and do not cause an accumulated pitch angle. A lager inclination occurs in T4 moment, and the pitch angles of sensor #1 and sensor #2 reach 2.838° and 2.795°. The sensors do not recover to the origin position as that in T2 and T3 moments, but maintain a pitch angle of 1.8°, which is the main source of the accumulated deformation during the monitoring period.

The sensors of monitoring node (#2–#5) experience slight pitch angle changes in the first day, which are the main accumulative changes during monitoring period. It can be considered that the deployment of the VA disturbs the surrounding soil, and the VA gradually stabilizes and couples well with the soil layer after a tidal cycle. Therefore, there is a slight inclination of the sensors in the first tidal cycle and then

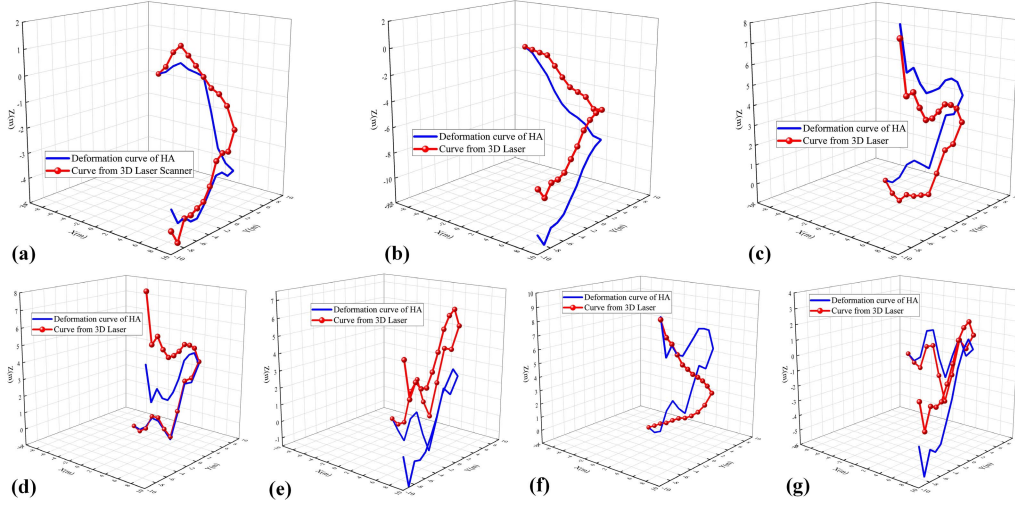


Fig. 15. Deformation curve obtained from HA and 3-D laser scanner from T1 to T7: (a) at 11:00 A.M. on January 25; (b) at 11:00 A.M. on January 26; (c) at 11:00 A.M. on January 27; (d) at 11:00 A.M. on January 28; (e) at 11:00 A.M. on January 29; (f) at 2:00 P.M. on January 30; and (g) at 14:00 A.M. on January 31.

TABLE V
Z-CORDINATES OBTAINED FROM HA

Sensor	Time 1	Time 2	Time 3	Time 4	Time 5	Time 6	Time 7
1	0	0	0	0	0	0	0
2	0.13	-0.37	0.01	-0.11	-0.62	-0.26	-0.37
3	0.40	-1.09	0.39	0.17	-1.14	-0.05	-0.05
4	0.56	-1.82	1.15	0.82	0.30	1.65	1.71
5	0.39	-2.90	1.45	0.74	0.81	2.53	1.84
6	0.31	-3.73	1.37	0.29	-0.41	2.07	0.13
7	0.22	-4.23	1.26	-0.18	-1.28	1.85	-1.02
8	-0.96	-4.49	2.67	1.46	0.60	3.74	0.46
9	-2.31	-4.85	4.05	3.33	2.58	5.49	1.71
10	-2.80	-5.57	4.19	3.49	2.32	5.39	0.62
11	-3.01	-5.72	5.15	4.59	3.43	6.85	1.11
12	-3.10	-6.03	5.85	5.30	3.91	8.18	1.82
13	-2.88	-6.56	6.08	5.30	3.35	8.38	1.27
14	-2.89	-7.33	6.08	5.07	2.79	8.47	0.23
15	-3.36	-8.41	5.82	4.17	1.62	7.96	-1.48
16	-3.81	-9.20	5.78	3.57	0.73	7.48	-2.75
17	-4.16	-10.03	5.77	3.26	-0.02	7.01	-3.97
18	-4.16	-10.41	6.27	3.47	-0.31	7.20	-4.30
19	-3.90	-10.54	7.02	4.08	-0.22	7.88	-4.00
20	-3.98	-11.54	6.89	3.48	-1.45	7.22	-5.50
21	-3.39	-10.61	8.93	5.51	0.29	9.80	-3.49

gradually keep stable. As shown in Fig. 16(b), the sensors in the reference monitoring node are relatively stable, except for the accumulative pitch angle in the first day. The pitch angle of all sensors is shown in Table VIII.

5) *Changes of Deformation Curve of the VA:* Since the terrain of the study area is flat and horizontal, no large-scale sliding occurs, but a circular slip surface exists in the shallow sediment layer [39]. The collected data shows that the boundary of the arc surface is at a deep about 10–40 cm. Expect for monitoring node 1 of the VA, the observed deformation of other nodes is small and not obvious. Thus, we focus on analyzing the deformation displacement characteristics of

node #1 only. As shown in Fig. 17, the deformation trend of node #1 presents three stages.

- Oscillation stage, which is the first six hours that from 10:00 to 15:00 on January 25. The top section of the VA vibrates continuously, and the vibration ranges in X- and Y-directions are -0.02 to 0.18 cm and -0.04 to 0.14 cm, respectively. The “vibration” phenomenon caused by the tidewater occurs in the first tidal cycle due to the poor coupling between the sensor array and the surrounding soil. In situ deployment of VA is completed at low tide, and the first high tide after that is on 15:00. As shown in Fig. 16(b), in the stable stage [gray rectangle in

TABLE VI
Z-CORDINATES OBTAINED FROM 3-D LASER SCANNER

Sensor	Time 1	Time 2	Time 3	Time 4	Time 5	Time 6	Time 7
1	0	0	0	0	0	0	0
2	0.32	-0.13	-0.57	-0.21	-0.24	0.26	-0.49
3	0.92	-0.25	-0.84	0.07	-0.01	0.56	-0.75
4	1.20	-0.34	-0.42	0.91	1.94	0.75	0.72
5	0.89	-1.03	-0.37	0.94	2.72	1.07	0.86
6	0.56	-1.76	-0.21	0.36	1.52	1.35	-0.98
7	0.21	-2.38	-0.06	0.00	0.78	1.51	-2.55
8	-0.15	-2.61	1.11	1.63	2.80	1.79	-0.75
9	-0.31	-2.86	2.37	3.48	4.79	2.19	1.52
10	-0.68	-3.61	2.76	3.74	4.80	2.82	1.07
11	-1.48	-3.54	3.90	4.73	6.14	3.79	1.97
12	-2.20	-3.62	4.63	5.56	7.06	4.41	2.85
13	-2.16	-3.97	4.88	5.80	6.81	4.90	2.58
14	-2.37	-4.55	5.01	5.92	6.18	5.27	1.92
15	-3.20	-5.52	4.77	5.65	5.08	5.59	0.64
16	-3.66	-6.25	4.57	5.51	4.14	6.04	-0.45
17	-3.79	-7.02	4.60	5.51	3.41	6.44	-1.39
18	-3.93	-7.31	5.23	5.99	3.48	7.20	-1.58
19	-3.93	-7.34	5.98	6.74	3.92	7.96	-1.40
20	-4.69	-8.19	5.91	6.41	3.15	8.47	-2.76
21	-4.16	-7.38	8.36	9.06	5.24	9.65	-0.87

TABLE VII
DEFORMATION ERRORS BETWEEN THE HA AND 3-D LASER SCANNER

Time	RMSE (mm)	MAE (mm)	ME (mm)
11:00am on Jan. 25 th	0.88	0.66	2.12
11:00am on Jan. 26 th	2.43	2.29	3.35
11:00am on Jan. 27 th	1.27	1.23	1.83
11:00am on Jan. 28 th	1.53	1.02	3.55
11:00am on Jan. 29 th	3.04	2.82	4.94
11:00am on Jan. 30 th	2.02	1.59	3.77
11:00am on Jan. 31 th	1.72	1.49	2.74

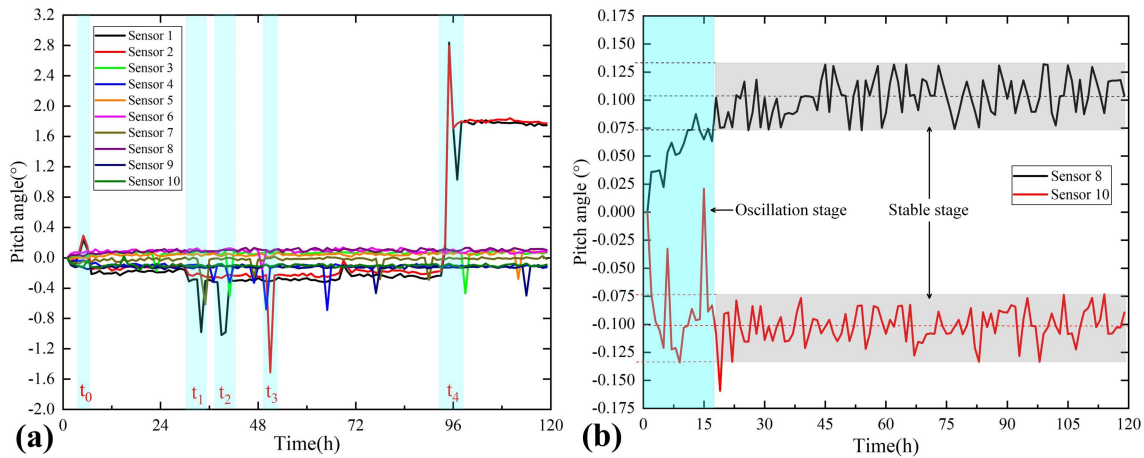


Fig. 16. (a) Pitch angle of all sensors on the VA. (b) Pitch angle of sensors #8 and #10.

Fig. 16(b)], the pitch angles of sensor 8 and sensor 10 are kept at about 0.1° and -0.1°, respectively, and the noise range of the sensors is about ±0.025°. However, in the

oscillation stage [blue rectangle in Fig. 16(b)], the monitoring nodes #4 and #5 do not directly reach the stable value and also experience the same oscillation stage as

TABLE VIII
PITCH ANGLE OF ALL SENSORS ON THE VA

Sensor	Max.ang ¹ (°)	Min.ang ² (°)	Mean.ang ³ (°)	Fin.ang ⁴ (°)
1	2.838	-1.018	0.181	1.748
2	2.795	-1.511	0.244	1.773
3	0.094	-0.504	0.051	0.073
4	0.000	-0.689	-0.117	-0.123
5	0.101	-0.278	0.042	0.086
6	0.138	-0.149	0.090	0.080
7	0.023	-0.612	-0.029	-0.016
8	0.132	0.000	0.096	0.104
9	0.000	-0.498	-0.126	-0.103
10	0.021	-0.159	-0.099	-0.089

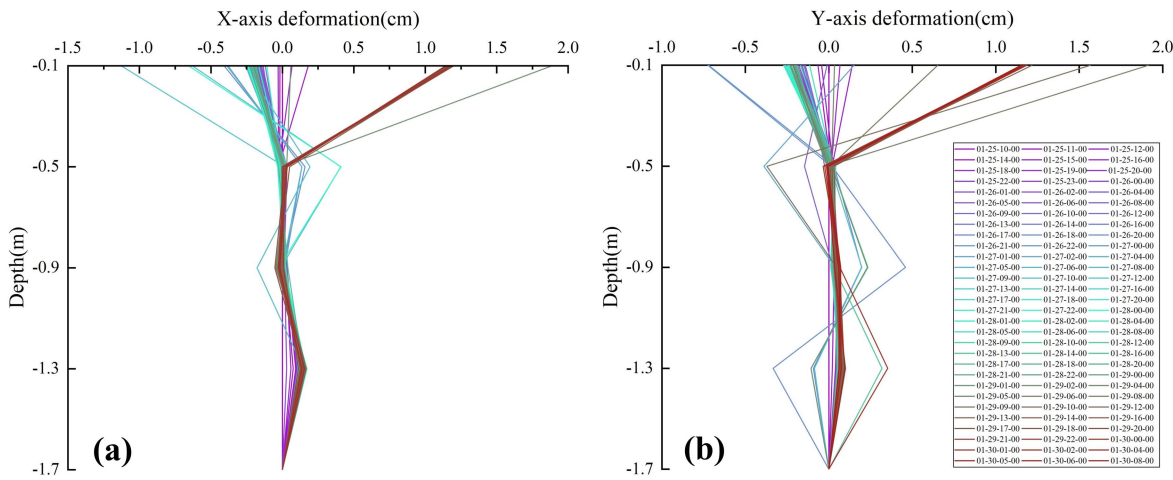


Fig. 17. Deformation shape of the VA. (a) X-axis deformation. (b) Y-axis deformation.

monitoring node #1, and the oscillation value is from 0° to 0.1° and -0.1°. Due to the damage of the soil during deployment process, the coupling relationship between MEMS sensor array and surrounding soil is poor. But, after a high tide, the suspended fine particles brought by the tidewater fill the gap between the sensor array and the soil, and the fine particles in the deep strata will also migrate upward under the action of buoyancy and PP. Thus, the coupling relationship between sensor array and surrounding soil becomes better and the vibration phenomenon no longer occurs after a high tide.

- 2) Slow accumulation stage. In this stage, the amount of the cumulative deformation reached -0.21 and -0.20 cm in X- and Y-axes, respectively. In addition, three sudden deformations with large displacements occur on 19:00 on January 26, 12:00 on January 27, and 2:00 on January 28, the amount of displacements reached -0.72 (Y-axis), -1.13 (X-axis), and -0.66 cm (X-axis), respectively. However, the sudden deformation is quickly recovered without generating a significant cumulative displacement.
- 3) Sudden deformation stage. A large deformation displacement suddenly generates in the positive direction on 8:00 on January 29. The deformation displacement changes from -0.21 to 1.91 cm in Y-axis, and from

-0.20 to 1.89 cm in X-axis. A small amount of deformation recovery occurs after the sudden deformation, but not completely recovers, and keeps at a positon of 1.19 and 1.18 cm in Y- and X-axes, respectively. Sudden deformation displacements occur with an hour, possible less time, even within a few minute. Therefore, the actual amount of deformation may be larger than collected data. If the data acquisition frequency is higher, the sudden deformation movements can be analyzed more accurately. Table IX shows the horizontal changes of all the sensors.

V. DISCUSSION

A. Data Acquisition Frequency of SN

During the in situ monitoring experiment, the sudden deformation and displacement occur both in HA and VA. Among them, the maximum uplifts and subsidence of HA are 21.53 and 25.77 mm, while the maximum deformations of VA in X- and Y-axes are 18.80 and 18.26 mm, respectively. Once the shallow sediment layer of tidal flat is failure, it will change to the plastic flow state due to liquefaction, and the soil particles will subject to a periodic vibration. The periodicity and vibration amplitude depend on the alternation of crests and troughs of tidewater and wave. The deformations and displacements of the tidal flat may be larger and faster than

TABLE IX
HORIZONTAL CHANGES OF ALL SENSORS ON THE VA

Direction	Sensor	Max.def (mm)	Min.def (mm)	Max.def.ph (mm)	Min.def.ph (mm)	Fin.def (mm)
Y-axis	1	19.14	-7.19	18.80	-7.85	11.52
	3	2.41	-3.89	4.26	-4.14	-0.91
	5	4.60	-1.91	2.63	-4.12	0.71
	7	3.53	-3.34	3.96	-4.25	0.61
	9	0	0	0	0	0
X-axis	2	-6.55	-11.27	18.26	-7.77	11.51
	4	4.11	-0.33	3.97	-3.92	0.30
	6	0.42	-1.77	1.67	-1.64	-0.17
	8	1.73	0.31	0.83	-0.87	1.35
	10	0	0	0	0	0

collected data, but since the data acquisition frequency of SN is set to once per hour, it may not be able to capture the maximum deformation. Because the deformations of terrain and strata in deep sea are very slow, research shown that the subsidence of the gas hydrate trial mining area is about 10 cm in ten days during trial mining [11], [40]. The power consumption is reduced as much as possible to realize long-term in situ deformation monitoring. In sleep mode, the SN works periodically. The power consumption in rest and work state is 0.72 and 8.28 W, respectively. In future, the data acquisition frequency of the SN can be adjusted to a higher data acquisition frequency to study the influence of tidewater and waves on the geological deformation of tidal flats.

B. Coupling Relationship Between SN and Surrounding Soil Layer

In the in situ monitoring of terrain and strata deformation, the coupling between the SN and surrounding soil must be considered. If the deformations of the SN and the soil are inconsistent when the terrain subsides or lifts and strata slides, the collected data will fail to truly reflect the deformation of the soil. The overall density of HA is increased, in order to prevent it from leaving the soil surface due to its own buoyancy, resulting in the failure of deformation measurement. In addition, the HA is buried inside the soil at a deep of 100 mm to ensure that no horizontal movement during high tide. Since the small particle size can be well-integrated into the soil, fine sand is buried between HA and surrounding soil layer to increase their coupling. However, if the soil sliding breaks the deformation coupling of SN and surrounding soil, especially during the liquefaction of shallow soil, the deformation of the soil will not be able to be captured due to the relative deformation between SN and soil. In addition, due to the bending stiffness of the SN, the surrounding soil will be squeezed and deformed when the SN is deformed. The observed deformations include the real deformation and the deformation caused by the extrusion of SN. Therefore, it is necessary to study the relationship of the deformation coupling between the SN and the soil, establish the deformation compensation model, and improve the deformation monitoring accuracy of the SN. Nevertheless,

the recorded tilt angle and deformation can objectively reflect the deformation of soil, providing a new method for seabed deformation monitoring [14], [41].

C. Feasibility of Monitoring in Deep-Sea Environment

The presented monitoring system aims to monitor the terrain and strata deformation of gas hydrate mining areas in SCS, where the temperature is within 2 °C–5 °C and the pressure is about 10–20 MPa [42]. The conditions of high pressure and low pressure must be considered for long-term operation of the monitoring system in deep sea. In the future study, the operating stability of the system should be tested in a simulated deep-sea environment. Moreover, self-contained monitoring system relies on lithium battery for power supply. At low temperature, the internal resistance of the lithium battery increases, and its capacity would be seriously reduced [43], [44]. Thus, in order to achieve long-term in situ monitoring, it is necessary to optimize the power management and reduce the power consumption. In addition, the mechanical properties of the seabed sediments in the aimed area should be considered. Studies have shown that the sediments in shallow strata in SCS are mostly silty clay and clay silt, with low shear strength and penetration resistance [45]. However, a small amount of hard carbonates still exists in the shallow strata of gas hydrate occurrence area and natural seepage region [46], and it may increase the difficulty of deployment. Therefore, the mechanical properties of the sediment should be investigated before the deployment of the SN.

VI. CONCLUSION

In this article, a monitoring system based on the MEMS SN is presented for monitoring the deformation of the terrain and shallow strata. The SN consists of an HA and a VA, with a terrain monitoring length of 20 m and a monitoring depth of 2 m. A reconstruction model of terrain and strata deformation was also proposed. To validate the monitoring system and the deformation reconstruction model, a field experiment was carried out on a tidal flat in Changzhi Island for one week. The principal conclusions are as follows.

- 1) The presented monitoring system based on MEMS SN can monitor the deformation of the terrain and strata

- simultaneously, and the developed prototype MEMS SN can monitor the terrain at a range of 20 m and the strata at a depth of 1.7 m.
- 2) A deformation reconstruction method based on the Euler rotation matrix and arc model is proposed, which can convert the three-axis acceleration into the horizontal and vertical deformations of the SN.
 - 3) According to the field experiment on the tidal flat in Changzhi Island, it is showed that the shallow soil undergoes periodic and reciprocating oscillations on the flat seabed, which is closely related to the tide variation. The terrain subsides at high tide and uplifts at low tide.
 - 4) The average deformation of the sensors on the HA was uplifted with a mean value uplift deformation is 3.61 mm, indicating that the overall deformation trend of the terrain in the study area is uplift.
 - 5) The deformation of the shallow soil layer could be divided into three stages: the oscillation stage, the slow accumulation stage, and the sudden deformation stage. The horizontal deformation mainly came from the sudden deformation stage, and the maximum deformation in X - and Y -axes is 18.80 and 18.26 mm, respectively.
 - 6) The shallow soil layer is severely deformed under the action of waves and tide, which undergoes a small-scale arc sliding, and the arc slide surface is at the depth of 10–40 cm.

The results show that our proposed monitoring method has great potential for in situ long-term deformation monitoring of seabed terrain and shallow strata. Nevertheless, further research is still required. The designed monitoring system is to be deployed to 30×30 m of seafloor and 3 m of strata around a slope zone in the SCS, and to achieve in situ monitoring of consecutive three months.

REFERENCES

- [1] C. D. Ruppel and W. F. Waite, "Timescales and processes of methane hydrate formation and breakdown, with application to geologic systems," *J. Geophys. Res., Solid Earth*, vol. 125, no. 8, pp. 1–43, Aug. 2020.
- [2] K. You, P. B. Flemings, A. Malinverno, T. S. Collett, and K. Darnell, "Mechanisms of methane hydrate formation in geological systems," *Rev. Geophys.*, vol. 57, no. 4, pp. 1146–1196, Dec. 2019.
- [3] R. Boswell and T. S. Collett, "Current perspectives on gas hydrate resources," *Energy Environ. Sci.*, vol. 4, no. 4, pp. 1206–1215, 2011.
- [4] Z. R. Chong, S. H. B. Yang, P. Babu, P. Linga, and X. S. Li, "Review of natural gas hydrates as an energy resource: Prospects and challenges," *Appl. Energy*, vol. 162, pp. 1633–1652, Jan. 2016.
- [5] C. Xu, J. Chen, H. Zhu, H. Liu, and Y. Lin, "Experimental research on seafloor mapping and vertical deformation monitoring for gas hydrate zone using nine-axis MEMS sensor tapes," *IEEE J. Ocean. Eng.*, vol. 44, no. 4, pp. 1090–1101, Oct. 2019.
- [6] Y. Q. Ge et al., "Development and sea trial of the terrain monitoring device based on MEMS sensing array," in *Proc. IOP Conf., Earth Environ. Sci.*, Oct. 2021, vol. 861, no. 7, Art. no. 072008.
- [7] L. Wan et al., "Submarine landslides, relationship with BSRs in the Dongsha area of south China Sea," *Petroleum Res.*, vol. 1, no. 1, pp. 59–69, Sep. 2016.
- [8] X. Wu, Q. Liang, M. Yun, Y. Shi, and M. Haeckel, "Submarine landslides and their distribution in the gas hydrate area on the North Slope of the south China sea," *Energies*, vol. 11, no. 12, p. 3481, 2018.
- [9] Y. Wang, J. Feng, X. Li, Y. Zhang, and H. Han, "Experimental investigation on sediment deformation during gas hydrate decomposition for different hydrate reservoir types," *Energy Proc.*, vol. 142, pp. 4110–4116, Dec. 2017.
- [10] H. Saito and T. Yokoyama, "Development of seafloor displacement monitoring system using a 3-component servo-accelerometer," in *Proc. OCEANS-MTS/IEEE Kobe Techno-Ocean*, Apr. 2008, pp. 1–4.
- [11] T. Yokoyama, M. Shimoyama, S. Matsuda, K. Tago, J. Takeshima, and Y. Nakatsuka, "Monitoring system of seafloor subsidence for methane hydrate production test," in *Proc. SPWLA 18th Formation Eval. Symp. Jpn.*, 2012, pp. 1–6.
- [12] J.-W. Park, S.-H. Sim, H.-J. Jung, and B. F. Spencer, Jr., "Development of a wireless displacement measurement system using acceleration responses," *Sensors*, vol. 13, no. 7, pp. 8377–8392, 2013.
- [13] C. Xu et al., "Design and laboratory testing of a MEMS accelerometer array for subsidence monitoring," *Rev. Sci. Instrum.*, vol. 89, no. 8, Aug. 2018, Art. no. 085103.
- [14] Z. H. Wang et al., "In situ observation of storm-wave-induced seabed deformation with a submarine landslide monitoring system," *Bull. Eng. Geol. Environ.*, vol. 77, pp. 1091–1102, Jul. 2018.
- [15] Y. Ge, J. Chen, C. Cao, J. He, Y. Sheng, and X. Zheng, "Design and test of a MEMS accelerometer array for submarine landslide displacement monitoring," *Mar. Technol. Soc. J.*, vol. 55, no. 1, pp. 5–16, Jan. 2021.
- [16] T. Uchimura et al., "Precaution and early warning of surface failure of slopes using tilt sensors," *Soils Found.*, vol. 55, no. 5, pp. 1086–1099, Oct. 2015.
- [17] V. Bennett, T. Abdoun, and M. Barendse, "Evaluation of soft clay field consolidation using MEMS-based in-place inclinometer-accelerometer array," *Geotech. Test. J.*, vol. 38, no. 3, pp. 290–302, 2015.
- [18] C. Griffith, P. Dare, and L. Danish, "Calibration enhancement of ShapeAccelArray technology for long term deformation monitoring applications," in *Proc. IEEE/ION Position, Location Navigat. Symp.*, May 2010, pp. 621–626.
- [19] D. W. Ha, J. M. Kim, Y. Kim, and H. S. Park, "Development and application of a wireless MEMS-based borehole inclinometer for automated measurement of ground movement," *Automat. Construct.*, vol. 87, pp. 49–59, Mar. 2018.
- [20] A. Segalini and C. Carini, "Underground landslide displacement monitoring: A new MMES based device," in *Landslide Science and Practice: Early Warning, Instrumentation and Monitoring*, vol. 2, C. Margottini, P. Canuti, and K. Sassa, Eds. Berlin, Germany: Springer, 2013, pp. 87–93.
- [21] G. L. Ooi et al., "An instrumented flume to characterize the initiation features of flow landslides," *Geotech. Test. J.*, vol. 37, no. 5, 2014, Art. no. 20130158.
- [22] J. Chen et al., "Experimental research on data synchronous acquisition method of subsidence monitoring in submarine gas hydrate mining area," *Sensors*, vol. 19, no. 19, pp. 4319–4333, 2019.
- [23] Z. Liang, D. Li, L. Yan, R. Zhao, and Y. Yuan, "Design and implementation of belt deviation detection sensor network based on RS485/Modbus," *J. Chin. Agricul. Mechanization*, vol. 4, pp. 217–220, May 2014.
- [24] C. Wan, "Research on multi-industry communication protocol conversion system," M.S. thesis, Nanchang Hangkong Univ., Nanchang, China, 2019, pp. 1–51.
- [25] C. Xu, J. Chen, Y. Ge, and M. Li, "Theoretical formulation/development of signal sampling with an equal arc length using the frame theorem," *EURASIP J. Adv. Signal Process.*, vol. 2022, no. 1, pp. 1–18, Dec. 2022.
- [26] C. Xu, J. Hu, J. Chen, Y. Ge, and R. Liang, "Sensor placement with two-dimensional equal arc length non-uniform sampling for underwater terrain deformation monitoring," *J. Mar. Sci. Eng.*, vol. 9, no. 9, p. 954, Sep. 2021.
- [27] Y. Zhang et al., "Design and testing of a flexible inclinometer probe for model tests of landslide deep displacement measurement," *Sensors*, vol. 18, no. 1, p. 224, 2018.
- [28] T. Hoshi and H. Shinoda, "Three-dimensional shape capture sheet using distributed six-axis sensors," in *Proc. 5th Int. Conf. Netw. Sens. Syst.*, Jun. 2008, pp. 156–161.
- [29] Y. Zhang, "Systematic research of landslide displacement monitoring based on inertial measurement," Ph.D. thesis, China Univ. Geosci., Wuhan, China, Tech. Rep., 2016, pp. 1–124.
- [30] Z. Xiong, M. Y. Wang, Z. G. Shan, Q. Yan, Y. J. Wang, and T. Li, "Physical and chemical characteristics of marine sediments in the offshore of Zhoushan," *Coastal Eng.*, vol. 38, no. 1, p. 6, 2019.
- [31] M. O. Green and G. Coco, "Review of wave-driven sediment resuspension and transport in estuaries," *Rev. Geophys.*, vol. 52, no. 1, pp. 77–117, 2014.
- [32] R. Wu, Z. Jiang, and C. Li, "Revisiting the tidal dynamics in the complex Zhoushan Archipelago waters: A numerical experiment," *Ocean Model.*, vol. 132, pp. 139–156, Dec. 2018.

- [33] G. B. Whitham, "The wave equation," in *Linear and Nonlinear Waves*. New York, NY, USA: Wiley, 1999, pp. 209–262.
- [34] T. Sakai, K. Hatanaka, and H. Mase, "Wave-induced effective stress in seabed and its momentary liquefaction," *J. Waterway, Port, Coastal, Ocean Eng.*, vol. 118, no. 2, pp. 202–206, 1992.
- [35] M. A. Foda, D. F. Hill, P. L. DeNeale, and C.-M. Huang, "Fluidization response of sediment bed to rapidly falling water surface," *J. Waterway, Port, Coastal, Ocean Eng.*, vol. 123, no. 5, pp. 261–265, Sep. 1997.
- [36] V. S. O. Kirca, B. M. Sumer, and J. Fredsøe, "Residual liquefaction of seabed under standing waves," *J. Waterway, Port, Coastal, Ocean Eng.*, vol. 139, no. 6, pp. 489–501, Nov. 2013.
- [37] B. Mutlu Sumer, F. Hatipoglu, J. Fredsøe, and S. Kaan Sumer, "The sequence of sediment behaviour during wave-induced liquefaction," *Sedimentology*, vol. 53, no. 3, pp. 611–629, Apr. 2006, doi: [10.1111/j.1365-3091.2006.00763.x](https://doi.org/10.1111/j.1365-3091.2006.00763.x).
- [38] H. Wang, H.-J. Liu, and M.-S. Zhang, "Pore pressure response of seabed in standing waves and its mechanism," *Coastal Eng.*, vol. 91, pp. 213–219, Sep. 2014.
- [39] G. Xu, Y. Sun, X. Wang, G. Hu, and Y. Song, "Wave-induced shallow slides and their features on the subaqueous yellow river delta," *Can. Geotech. J.*, vol. 46, no. 12, pp. 1406–1417, Dec. 2009.
- [40] T. Yokoyama, M. Shimoyama, S. Matsuda, K. Tago, and J. Takeshima, "Monitoring system for seafloor deformation during methane hydrate production test," in *Proc. 10th ISOPE Ocean Mining Gas Hydrates Symp.*, 2013, pp. 132–135.
- [41] Z. Wang et al., "Wave-induced seafloor instabilities in the subaqueous Yellow River Delta—Initiation and process of sediment failure," *Land-slides*, vol. 17, no. 8, pp. 1849–1862, Aug. 2020.
- [42] J. Li and J. Lan, "Seasonal variation of deep vertical velocity in the south China Sea," *Ocean Model.*, vol. 172, Apr. 2022, Art. no. 101990.
- [43] Z. Lei, C. Zhang, J. Li, G. Fan, and Z. Lin, "A study on the low-temperature performance of lithium-ion battery for electric vehicles," *Automot. Eng.*, vol. 35, no. 10, pp. 927–933, 2013.
- [44] Q. S. Zhong, S. J. Li, B. Huang, J. H. Ma, and H. Li, "Discharge and temperature characteristics of li-ion batteries," *J. Univ. Electron. Sci. Technol. China*, vol. 43, no. 2, pp. 311–314, 2014.
- [45] C. Q. Zhu et al., "Preliminary study of physical and mechanical properties of surface sediment in northern south China Sea," *J. Eng. Geol.*, vol. 25, no. 6, p. 1566, 2017.
- [46] L. Bin, "Gas and gas hydrate distribution around seafloor mound in the Dongsha area, North Slope of the south China Sea," *Acta Oceanol. Sinica*, vol. 39, no. 3, pp. 68–75, 2017.



Chen Cao received the B.S. degree in automation from Zhejiang University, Hangzhou, China, in 2018. He is currently pursuing the Ph.D. degree in marine technology and engineering with Zhejiang University, Zhoushan, China.

He has authored five Science Citation Index (SCI) articles, and holds two Chinese invention patents and one U.S. utility patent. His research interests include seafloor mapping, deformation monitoring, and underwater cable shape detection.



Peng Zhou received the M.S. degree in control engineering from the Wuhan University of Technology, Wuhan, China, in 2012.

He is currently an Electrical Engineer with the Institute of Ocean Engineering and Technology, Zhejiang University, Zhoushan, China. His research interests include circuit design, mechanical system control, and signal acquisition.



Chunying Xu received the Ph.D. degree in marine information science and technology from Zhejiang University, Zhoushan, China, in 2019.

She is currently a Lecturer with the Department of Engineering, Shantou University, Shantou, China. Her research interests include the terrain deformation monitoring, underwater cable health monitoring, smart instrument, and signal processing technology.



Yongqiang Ge received the B.S. degree from the Ocean College, Zhejiang University, Zhoushan, China, in 2019, where he is currently pursuing the Ph.D. degree in marine technology and engineering.

He has authored more than ten articles in the research field of seafloor subsidence monitoring and landslide monitoring. He holds three invention patents. His research mainly focused on the research of seafloor deformation monitoring technology and equipment.



Hai Zhu received the B.S. degree in mechanical manufacturing and automation from the China University of Petroleum (East China), Qingdao, China, in 2017. He is currently pursuing the Ph.D. degree in marine technology and engineering with Zhejiang University, Zhoushan, China.

He has authored two Science Citation Index articles and holds four Chinese invention patents. His research interests include submarine pipeline mapping and repair, pressure maintaining transfer of natural gas hydrate (NGH), and rheology.



Jiwang Chen received the Ph.D. degree in geo-tech engineering from the Construction Engineering College, Jilin University, Changchun, China, in 2007.

He is currently the Director of the Institute of Ocean Engineering, Zhejiang University, Zhoushan, China. He has authored more than 100 articles in the research field of ocean technology and equipment. He holds 60 invention patents. His research mainly focused on the research of pressure sampling technology, pressure transfer and treatment technology, and seafloor subsidence monitoring technology.



Xiaoxiao Zhou received the B.S. degree in marine engineering and technology from Zhejiang University, Hangzhou, China, in 2022. He is currently pursuing the M.S. degree with the Ocean College, Zhejiang University, Zhoushan, China.

His current research interests include ocean monitoring, deep-ocean sampling, and control system.